SCIENCE CHINA
Information Sciences

• RESEARCH PAPER •

November 2026, Vol. 69, Iss. 11, 210204:1–210204:15
https://doi.org/10.1007/s11432-026-5237-5

Special Topic: Intelligent Characterization and Modeling for Complex Systems

Turing patterns on multiplex-networked activator-inhibitor systems with multiplicative noise

Haifeng DAI[1,2], Guanghui WEN[3*], Guanrong CHEN[2] & Yongzheng SUN[4,5]

[1]*School of Cyber Science and Engineering, Southeast University, Nanjing 210096, China*
[2]*Department of Electrical Engineering, City University of Hong Kong, Hong Kong 999077, China*
[3]*School of Automation, Southeast University, Nanjing 210096, China*
[4]*School of Mathematics, China University of Mining and Technology, Xuzhou 221008, China*
[5]*Shenzhen Research Institute, China University of Mining and Technology, Shenzhen 518057, China*

Received 4 June 2026/Revised 8 October 2026/Accepted 19 October 2026/Published online 4 November 2026

Abstract The emergence of Turing patterns is often the collective result of multi-layered interactions and ubiquitous environmental fluctuations. While Turing instability has been extensively studied in single-layered and deterministic networks, the synergistic role of multiplex topology and multiplicative noise remains unexplored. This paper proposes a multiplex-networked stochastic activator-inhibitor system, where state-dependent multiplicative noise driven by mutually independent edge noise processes is incorporated into both intra-layer and inter-layer diffusion processes, with an intensity proportional to the density differences between neighboring nodes. By utilizing the stability theorem of stochastic differential equations, a sufficient condition for almost sure convergence to the uniform stationary state is derived. The results reveal that multiplicative noise affects pattern onset non-monotonically, while stronger noise promotes pattern formation and reduces the observed hysteresis width. In addition, inter-layer coupling can exert a complex, non-monotonic influence on Turing instability, and the critical thresholds may exhibit saturation at strong coupling under certain parameter settings. Finally, topological analysis reveals pronounced robustness of the forward threshold across the examined Pure-BA configurations, where pattern onset is governed predominantly by hub-localized critical modes. This behavior contrasts with the greater sensitivity to connectivity and inter-layer architecture observed in Pure-ER and Pure-WS networks. These findings provide new insights into the constructive role of noise and multiplex architecture in driving network self-organization.

Keywords Turing pattern, multiplex network, multiplicative noise, activator-inhibitor system, stochastic stability

Citation Dai H F, Wen G H, Chen G R, et al. Turing patterns on multiplex-networked activator-inhibitor systems with multiplicative noise. Sci China Inf Sci, 2026, 69(11): 210204, https://doi.org/10.1007/s11432-026-5237-5

1 Introduction

Reaction-diffusion systems have been widely used to describe the dynamics of various biological, chemical, and ecological processes [1–7]. A notable self-organized structure within such systems is the well-known Turing pattern, which emerges from the diffusion-driven instability of a uniformly stable state [8–10]. As a fundamental class of reaction-diffusion models, activator-inhibitor systems have been extensively studied to elucidate the underlying mechanisms of such pattern formation. In these systems, the activator promotes the production of itself and the inhibitor, whereas the inhibitor suppresses the production of both species [9].

Natural systems are rarely isolated; rather, they are highly interconnected, interacting through complex network topologies that facilitate the emergence of novel dynamical phenomena [11–18]. Early studies on Turing patterns in discrete spatial domains were focused on regular lattices and small-scale networks, providing fundamental insights into network-organized pattern formation [19–22]. However, subsequent research revealed that reaction-diffusion processes on scale-free networks exhibit fundamentally different dynamics compared to those on regular lattices [23]. The pioneering work in [24] successfully extended Turing's theory to large, undirected complex networks, laying a theoretical foundation for this expanding field. Subsequent investigations into directed networks uncovered topologically driven instabilities and pattern formation mechanisms completely distinct from their undirected counterparts [25]. Building upon these foundational studies, Turing instability on complex networks has been extensively explored, revealing a rich diversity of pattern-forming mechanisms and exotic self-organized phenomena [26–29].

The above studies on network-organized Turing patterns assume that the activator and the inhibitor share identical interaction topologies. Recent efforts have relaxed this constraint, exploring scenarios where different

* Corresponding author (email: ghwen@seu.edu.cn)

© Science China Press 2026

species disperse through distinct topological structures [30–33]. While these extensions enrich single-layer dynamics, a more realistic situation is that populations and substances rarely disperse through a single, isolated medium. For example, rumors propagate simultaneously across multiple social media platforms, viruses transmit via diverse contact routes, and ecological species navigate on both surface habitats and subterranean corridors concurrently. To address these ubiquitous real-world complexities, research has begun to consider multiplex networks [34–37]. To date, such multiplex frameworks have been studied [38], revealing that inter-layer coupling, which represents the interaction between adjacent layers, can actively promote Turing instability and seed the formation of self-organized patterns.

Recognizing the ubiquity of fluctuations in real-world environments, the influence of noise on Turing patterns has garnered significant attention [39–42]. Contrary to the traditional view of various noise as a mere disruptive perturbation, research demonstrates that it can actively facilitate self-organized behavior. For instance, demographic and intrinsic fluctuations have been shown to induce robust stochastic Turing patterns, which expand the conditions for pattern formation and relax the stringent parameter constraints inherent in deterministic models [43, 44]. Both theoretical analyses and experimental observations demonstrate that stochastic fluctuations, typically modeled as additive noise, can significantly enlarge the parameter space conducive to Turing instability [5, 45]. While much research in the recent literature focuses on additive noise, which operates independently of the system's states, fluctuations in many real-world systems are inherently multiplicative. In these scenarios, the noise intensity is coupled to the system's states, a characteristic that can induce qualitatively different dynamics compared to additive noise.

Recent studies have considered the effects of multiplicative noise and reported qualitatively different behaviors. Increasing multiplicative noise intensity can enhance the stability of the uniform stationary state and suppress Turing pattern formation [46]. In the stochastic Brusselator studied by Khan et al. [47], this suppression occurs when the noise intensities acting on both species are equal and sufficiently large. More interestingly, when the noise acts only on either the activator or the inhibitor, it can instead destabilize the system and facilitate Turing pattern formation [47].

Existing studies of multiplicative noise have largely focused on specific formulations in which noise intensity is defined with respect to deviations from a prescribed uniform stationary state and the same noise process is applied throughout the system. Whether their conclusions remain valid for stochastic fluctuations driven by local state differences is still unclear. On the other hand, multiplex topology determines the intra-layer and inter-layer pathways along which local state differences drive both deterministic diffusion and stochastic fluctuations. These fluctuations, in turn, modify the state differences on which their amplitudes depend, thereby coupling the effects of topology, diffusion, and noise. It therefore remains unclear whether stability conclusions established for deterministic multiplex systems remain valid in this stochastic setting. Moreover, a unified stability framework capable of jointly characterizing the effects of network topology, diffusion parameters, and state-dependent noise remains lacking.

Motivated by these issues, this work investigates the stability and Turing pattern formation of multiplex-networked activator-inhibitor systems subject to multiplicative noise driven by local state differences, combining theoretical analysis with numerical simulations to elucidate their joint effects. The main contributions are summarized as follows.

(1) We formulate a multiplex-networked activator-inhibitor system with state-dependent multiplicative noise driven by mutually independent edge noise processes. The noise acts on both intra-layer and inter-layer diffusion processes, with its intensity proportional to the state differences between neighboring nodes, thereby capturing stochastic fluctuations arising from local interactions.

(2) Based on the stability theory of stochastic differential equations, we derive a sufficient condition for almost sure convergence to the uniform stationary state. The resulting criterion incorporates the local node dynamics, diffusion parameters, spectral properties of the network topology, and noise intensity within a unified analytical framework, providing a theoretical basis for qualitatively characterizing their combined effects on system stability.

(3) Numerical simulations show that noise affects pattern onset non-monotonically and reduces the observed hysteresis width. Even with the dynamical parameters fixed, inter-layer coupling can exert a non-monotonic influence on Turing pattern formation, and the critical thresholds may exhibit saturation.

(4) By comparing the Turing thresholds across different network topologies, network sizes, and numbers of layers, we find weak scale sensitivity of the forward threshold across the examined Pure-BA configurations. The critical spectral positions and hub localization provide a structural explanation for this robustness.

The remainder of this paper is organized as follows. Section 2 formulates the deterministic and stochastic multiplex-networked activator-inhibitor systems. A rigorous stochastic stability analysis is provided in Section 3. Section 4 presents numerical simulations, and Section 5 concludes the paper.

Notation. For a sequence of numbers $\{a_i\}_{i=1}^N$, let $\mathrm{diag}(\{a_i\}_{i=1}^N)$ be a diagonal matrix with entries $a_1, a_2, \ldots, a_N$,

and define the column vector $[a_i]_{i=1}^N = [a_1, a_2, \ldots, a_N]^\top$. In particular, let $I_N = \mathrm{diag}(\{1\}_{i=1}^N)$, $\mathbf{1}_N = [1]_{i=1}^N$, and $\mathbf{0}_N = [0]_{i=1}^N$. For a collection of vectors $a_i \in \mathbb{R}^m$, $[a_i]_{i=1}^N = [a_1^\top, a_2^\top, \ldots, a_N^\top]^\top \in \mathbb{R}^{mN}$ denotes their concatenated block column vector. Similarly, for matrices $A_i \in \mathbb{R}^{m\times m}$, $\mathrm{diag}(\{A_i\}_{i=1}^N)$ denotes a block diagonal matrix with $A_1, A_2, \ldots, A_N$ on its main diagonal.

2 Activator-inhibitor systems on multiplex networks

The single-layered networked activator-inhibitor systems can be described as follows [24]:

$$\dot{u}_i = f(u_i, v_i) + \alpha \sum_{j=1}^N a_{ij}(u_j - u_i), \qquad \dot{v}_i = g(u_i, v_i) + \sigma\alpha \sum_{j=1}^N a_{ij}(v_j - v_i),$$

where u_i and v_i denote the densities of the activator and inhibitor on the i-th node ($i = 1, \ldots, N$), respectively. The nonlinear functions f and g represent the local reaction dynamics. The parameter $\alpha > 0$ is the diffusion coefficient, while $\sigma > 0$ denotes the ratio of the inhibitor's diffusion rate to that of the activator. Furthermore, a_{ij} represents the entries of the adjacency matrix that captures the network's topological structure, with $a_{ij} = 1$ if an edge exists between the i-th and j-th nodes, and $a_{ij} = 0$ otherwise.

Turing instability is conventionally investigated by analyzing the system dynamics within a small neighborhood $\mathcal{B} = \{(u-u^*)^2 + (v-v^*)^2 \leqslant \epsilon^2\} \subset \mathbb{R}^2$ of the uniform stationary state (u^*, v^*), where $\epsilon > 0$ is a sufficiently small constant. To facilitate the theoretical analysis, the following assumption is presented on the nonlinear functions f and g, which is commonly adopted in the study of Turing instability of activator-inhibitor systems.

Assumption 1. The local dynamics are assumed to have a uniform stationary state (u^*, v^*) satisfying that $f(u^*, v^*) = 0$ and $g(u^*, v^*) = 0$, and (u^*, v^*) is assumed stable, i.e., $f_u + g_v < 0$ and $f_u g_v - f_v g_u > 0$, where f_u, f_v, g_u and g_v are the partial derivatives of f and g with respect to u and v, respectively.

2.1 Multiplex-networked activator-inhibitor systems

In natural ecosystems, species rarely disperse through a single, isolated medium. For instance, interacting populations such as predators and prey often navigate on surface habitats while simultaneously utilizing subterranean corridors, thereby creating a complex, layered relational topology. Recent advances in network studies elegantly captured these real-world intricacies through the framework of multiplex networks, where identical sets of nodes reside in distinct layers and are linked by inter-layer couplings. Despite the ubiquity of such multifaceted structures, our understanding of how inter-layer coupling affects the Turing instability of activator-inhibitor systems remains highly constrained.

Consider an activator-inhibitor system on a multiplex network with K layers sharing the same set of N nodes, as illustrated in Figure 1(a). Each layer has its own intra-layer topology, while inter-layer edges connect only corresponding node replicas. The inter-layer topology is undirected, connected, and without self-loops; complete and path-type examples are shown in Figures 1(b) and (c), respectively. The local dynamics on the multiplex network are described by

$$\begin{aligned}
\dot{u}_i^{(k)} &= f(u_i^{(k)}, v_i^{(k)}) + \alpha \sum_{j=1}^N a_{ij}^{(k)}(u_j^{(k)} - u_i^{(k)}) + \beta \sum_{l=1}^K b_{kl}(u_i^{(l)} - u_i^{(k)}),\\
\dot{v}_i^{(k)} &= g(u_i^{(k)}, v_i^{(k)}) + \sigma\alpha \sum_{j=1}^N a_{ij}^{(k)}(v_j^{(k)} - v_i^{(k)}) + \sigma\beta \sum_{l=1}^K b_{kl}(v_i^{(l)} - v_i^{(k)}),
\end{aligned} \tag{1}$$

where $u_i^{(k)}$ and $v_i^{(k)}$ denote the densities of the activator and inhibitor on the i-th node in the k-th layer ($i = 1, \ldots, N; k = 1, \ldots, K$), respectively. The parameter $\beta > 0$ is the inter-layer diffusion coefficient. Here, β/α is called the inter-layer coupling strength. Similar to single-layer networks, $a_{ij}^{(k)}$ and b_{kl} are binary entries that capture the topological structures by characterizing the intra-layer and inter-layer connectivity, respectively. Specifically, $a_{ij}^{(k)} = 1$ if an edge exists between the i-th and j-th nodes in the k-th layer, and $b_{kl} = 1$ if the nodes in layers k and l are connected via an inter-layer edge; otherwise, they are zero.

Following the typical formalism [48], the multiplex network is represented by the intra-layer and inter-layer adjacency matrices $A^{(k)} = [a_{ij}^{(k)}]_{N\times N}$ and $B = [b_{kl}]_{K\times K}$. Furthermore, the intra-layer and inter-layer Laplacian

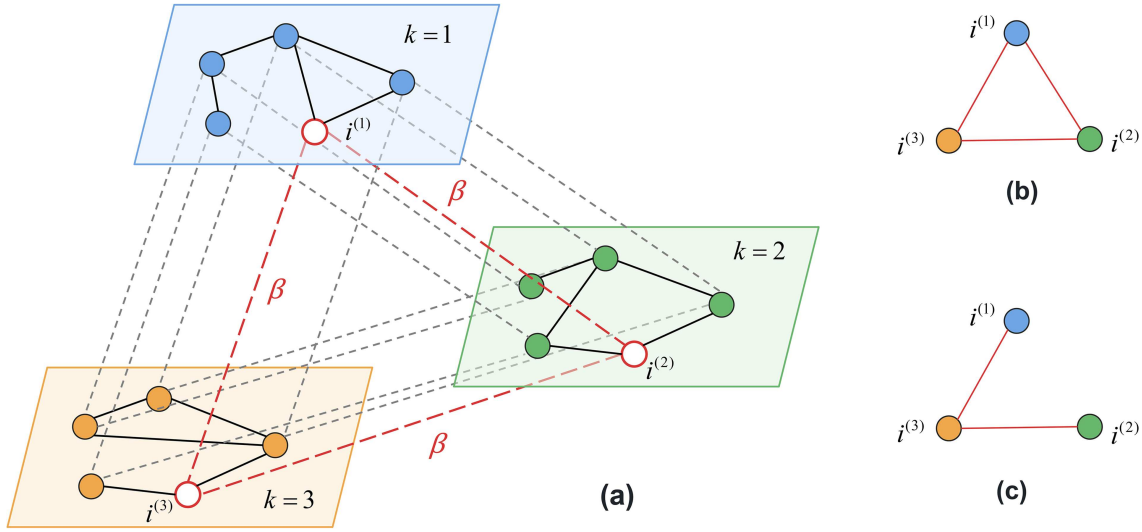

Figure 1 (Color online) Schematic representation of a multiplex network and its inter-layer coupling structures. (a) A three-layer multiplex network, where each layer has its own intra-layer topology represented by black solid edges. Corresponding replicas of the same node across layers are connected by inter-layer couplings, shown by gray dashed edges; the highlighted nodes $i^{(1)}$, $i^{(2)}$, and $i^{(3)}$ illustrate inter-layer links with diffusion coefficient β. (b) Complete inter-layer topology, in which every pair of layers is connected. (c) Path-type inter-layer topology, in which the layers are connected sequentially through an intermediate layer.

matrices are defined by $L^{(k)} = D^{(k)} - A^{(k)}$ and $L^I = D^I - B$ where $D^{(k)} = \mathrm{diag}(\{\sum_{j=1}^N a_{ij}^{(k)}\}_{i=1}^N)$ and $D^I = \mathrm{diag}(\{\sum_{l=1}^K b_{kl}\}_{k=1}^K)$ are the degree matrices of $A^{(k)}$ and B, respectively. Let $u = [(u^{(k)})]_{k=1}^K$ and $v = [v^{(k)}]_{k=1}^K$, where $u^{(k)} = [u_i^{(k)}]_{i=1}^N$ and $v^{(k)} = [v_i^{(k)}]_{i=1}^N$, and similarly,

$$f(u,v) = [f(u^{(k)}, v^{(k)})]_{k=1}^K, \quad g(u,v) = [g(u^{(k)}, v^{(k)})]_{k=1}^K,$$
$$f(u^{(k)}, v^{(k)}) = [f(u_i^{(k)}, v_i^{(k)})]_{i=1}^N, \quad g(u^{(k)}, v^{(k)}) = [g(u_i^{(k)}, v_i^{(k)})]_{i=1}^N.$$

Then, system (1) can be rewritten in a compact form as

$$\dot{u} = f(u,v) - \alpha\mathcal{L}u, \ \ \dot{v} = g(u,v) - \sigma\alpha\mathcal{L}v,$$

where $\mathcal{L} = \mathcal{L}^L + \beta/\alpha\mathcal{L}^I$ is the full super-Laplacian, $\mathcal{L}^L = \mathrm{diag}(\{L^{(k)}\}_{k=1}^K)$ is the intra-layer super-Laplacian, and $\mathcal{L}^I = L^I \otimes I_N$ is the inter-layer super-Laplacian.

Assumption 2. The intra-layer and inter-layer networks are undirected and connected without self-loops.

2.2 Multiplex-networked activator-inhibitor systems with noise

The interactions between nodes are usually influenced by various perturbations, including environmental fluctuations, measurement errors, and intrinsic stochasticity, which are modeled as state-dependent multiplicative noise in this paper.

Incorporating multiplicative noise into both intra-layer and inter-layer interactions, the density measurements of intra-layer neighboring nodes are perturbed from $u_j^{(k)}$ and $v_j^{(k)}$ to $u_j^{(k)} + \eta_{ij}^{(k)}(u_j^{(k)} - u_i^{(k)})\xi_{ij}^{(k)}$ and $v_j^{(k)} + \eta_{ij}^{(k)}(v_j^{(k)} - v_i^{(k)})\xi_{ij}^{(k)}$, and similarly, the density measurements of inter-layer neighboring nodes are perturbed from $u_i^{(l)}$ and $v_i^{(l)}$ to $u_i^{(l)} + \eta_i^{(kl)}(u_i^{(l)} - u_i^{(k)})\xi_i^{(kl)}$ and $v_i^{(l)} + \eta_i^{(kl)}(v_i^{(l)} - v_i^{(k)})\xi_i^{(kl)}$, where $\eta_{ij}^{(k)}$ and $\eta_i^{(kl)}$ are the intensities of the noise, $\xi_{ij}^{(k)}$ and $\xi_i^{(kl)}$ are standard independent Gaussian white noise. For simplicity, it is assumed that the noise and its intensity are homogeneous on both the activator and inhibitor components, and $\eta_{ij}^{(k)} = \eta_{ji}^{(k)} \geqslant 0$ and $\eta_i^{(kl)} = \eta_i^{(lk)} \geqslant 0$ are constant edge-specific noise coupling intensities. Consequently, the stochastic multiplex system takes the Itô form

$$
\begin{aligned}
\mathrm{d}u_i^{(k)} &= \left[f(u_i^{(k)}, v_i^{(k)}) + \alpha \sum_{j=1}^{N} a_{ij}^{(k)} (u_j^{(k)} - u_i^{(k)}) + \beta \sum_{l=1}^{K} b_{kl} (u_i^{(l)} - u_i^{(k)}) \right] \mathrm{d}t \\
&\quad + \alpha \sum_{j=1}^{N} a_{ij}^{(k)} \eta_{ij}^{(k)} (u_j^{(k)} - u_i^{(k)}) \, \mathrm{d}W_{ij}^{(k)} + \beta \sum_{l=1}^{K} b_{kl} \eta_i^{(kl)} (u_i^{(l)} - u_i^{(k)}) \, \mathrm{d}W_i^{(kl)}, \\
\mathrm{d}v_i^{(k)} &= \left[g(u_i^{(k)}, v_i^{(k)}) + \sigma\alpha \sum_{j=1}^{N} a_{ij}^{(k)} (v_j^{(k)} - v_i^{(k)}) + \sigma\beta \sum_{l=1}^{K} b_{kl} (v_i^{(l)} - v_i^{(k)}) \right] \mathrm{d}t \\
&\quad + \sigma\alpha \sum_{j=1}^{N} a_{ij}^{(k)} \eta_{ij}^{(k)} (v_j^{(k)} - v_i^{(k)}) \, \mathrm{d}W_{ij}^{(k)} + \sigma\beta \sum_{l=1}^{K} b_{kl} \eta_i^{(kl)} (v_i^{(l)} - v_i^{(k)}) \, \mathrm{d}W_i^{(kl)}.
\end{aligned} \tag{2}
$$

Here, $W_{ij}^{(k)}$ and $W_i^{(kl)}$ are standard Wiener processes whose formal time derivatives are $\xi_{ij}^{(k)}$ and $\xi_i^{(kl)}$, respectively. Processes associated with distinct undirected edges are mutually independent, whereas $W_{ij}^{(k)} = W_{ji}^{(k)}$ and $W_i^{(kl)} = W_i^{(lk)}$.

To facilitate the stability analysis, we group the activator and inhibitor components into a two-dimensional state vector at each node. Defining the node state $x_i^{(k)} = [u_i^{(k)}, v_i^{(k)}]^\top$ and the uniform stationary state $x^* = [u^*, v^*]^\top$, and letting $x^{(k)} = [x_i^{(k)}]_{i=1}^N$ and $x = [x^{(k)}]_{k=1}^K$, system (1) is reformulated as follows:

$$
\dot{x_i}^{(k)} = h(x_i^{(k)}) + \alpha\varsigma \sum_{j=1}^{N} a_{ij}^{(k)} (x_j^{(k)} - x_i^{(k)}) + \beta\varsigma \sum_{l=1}^{K} b_{kl} (x_i^{(l)} - x_i^{(k)}),
$$

where $\varsigma = \mathrm{diag}\{1, \sigma\}$, $h(x_i^{(k)}) = [f(x_i^{(k)}), g(x_i^{(k)})]^\top$, and its compact form can be formulated as

$$
\dot{x} = h(x) - \alpha(\mathcal{L}^L \otimes \varsigma)x - \beta(\mathcal{L}^I \otimes \varsigma)x = h(x) - \alpha(\mathcal{L} \otimes \varsigma)x.
$$

According to [48], $\mathcal{L}$ has one zero eigenvalue with eigenvector $\mathbf{1}_{NK}$, and the other eigenvalues $\lambda_i, i = 2, \ldots, NK$, are all positive. Although the stochastic system can be linearized around the uniform stationary state, the eigenvalues of the deterministic drift matrix alone are insufficient to determine stability in the presence of multiplicative noise. Therefore, we seek a solution from the stability theory of stochastic systems.

Let $B^{(k)} \in \mathbb{R}^{N \times m_k}$ and $B^{\mathrm{layer}} \in \mathbb{R}^{K \times m_{\mathrm{layer}}}$ denote the signed incidence matrices of layer k and the interlayer graph, respectively, where m_k and m_{layer} are the corresponding numbers of undirected edges. Each edge is represented by one column with entries $+1$ and -1 at its endpoints and zero elsewhere. The incidence matrices of the multiplex network are then

$$
B_L = \mathrm{diag}\left(B^{(1)}, \ldots, B^{(K)}\right), \qquad B_I = B^{\mathrm{layer}} \otimes I_N.
$$

Thus $\mathcal{L}^L = B_L B_L^\top$ and $\mathcal{L}^I = B_I B_I^\top$. Let $m_L = \sum_{k=1}^K m_k$ and $m_I = N m_{\mathrm{layer}}$ be the numbers of intra-layer and individual inter-layer edges, respectively. Each column of B_I corresponds to one edge between node replicas and hence one independent noise channel. Defining $\mathsf{B} = [B_L \;\; B_I]$ and $m = m_L + m_I$, we obtain

$$
C = \mathrm{diag}\left(I_{m_L}, \frac{\beta}{\alpha} I_{m_I}\right), \qquad \mathcal{L} = \mathsf{B} C \mathsf{B}^\top.
$$

Let b_q be the q-th column of B and $c_q = C_{qq}$, and define $A_q = c_q(b_q b_q^\top \otimes \varsigma)$ for $q = 1, \ldots, m$. Then $\sum_{q=1}^m A_q = \mathcal{L} \otimes \varsigma$, and let $\eta_q \geqslant 0$ be the noise intensity of the corresponding edge in (2). Then system (2) takes the compact form

$$
\mathrm{d}x = [h(x) - \alpha(\mathcal{L} \otimes \varsigma)x] \, \mathrm{d}t - \alpha \sum_{q=1}^{m} \eta_q A_q x \, \mathrm{d}W_q(t). \tag{3}
$$

Here, $\{W_q\}_{q=1}^m$ are the mutually independent standard Wiener processes associated with the intra-layer and interlayer edges in (2).

To analyze the dynamics within $\mathcal{B}$, we impose the following local one-sided Lipschitz condition on the reaction function $h(\cdot)$.

Assumption 3. The reaction function h is locally Lipschitz on an open neighborhood containing the closed ball $\mathcal{B}$ around the uniform stationary state x^*. Moreover, there exists a constant $\ell \in \mathbb{R}$ such that

$$(x-y)^\top [h(x)-h(y)] \leqslant \ell \|x-y\|^2, \qquad x, y \in \mathcal{B}.$$

3 Stochastic stability analysis

System (3) is said to converge almost surely to the uniform stationary state x^* if, for any initial state $x_0 \in \mathcal{B}^{NK}$,

$$\mathbb{P}\left\{\lim_{t\to\infty} x_i^{(k)}(t) = x^*\right\} = 1.$$

Conventionally, a small perturbation $\delta x_i^{(k)} = [\delta u_i^{(k)}, \delta v_i^{(k)}]$ is introduced to the uniform stationary state x^* such that $x_i^{(k)} = x^* + \delta x_i^{(k)}$, and then the stability analysis of the perturbed system is conducted. Hence, we approach this differently by letting $\bar{x} = \frac{1}{NK}\sum_{k=1}^{K}\sum_{i=1}^{N} x_i^{(k)}$, and $e_i^{(k)} = x_i^{(k)} - \bar{x}$. We first establish almost sure convergence of the synchronization errors, $\mathbb{P}\{\lim_{t\to\infty} e_i^{(k)}(t) = \mathbf{0}_2\} = 1$, and subsequently examine convergence of the synchronized dynamics to the uniform stationary state x^*. The synchronization error system takes the following form:

$$\begin{aligned}\mathrm{d}e_i^{(k)} = &\left[h(x_i^{(k)}) - \frac{1}{NK}\sum_{r=1}^{K}\sum_{j=1}^{N} h(x_j^{(r)}) + \alpha\varsigma\sum_{j=1}^{N} a_{ij}^{(k)}(e_j^{(k)} - e_i^{(k)}) + \beta\varsigma\sum_{l=1}^{K} b_{kl}(e_i^{(l)} - e_i^{(k)})\right]\mathrm{d}t \\ &+ \alpha\varsigma\sum_{j=1}^{N} a_{ij}^{(k)}\eta_{ij}^{(k)}(e_j^{(k)} - e_i^{(k)})\,\mathrm{d}W_{ij}^{(k)} + \beta\varsigma\sum_{l=1}^{K} b_{kl}\eta_i^{(kl)}(e_i^{(l)} - e_i^{(k)})\,\mathrm{d}W_i^{(kl)}.\end{aligned}$$

To obtain its compact form, define the projection matrix $P = I_{NK} - \frac{1}{NK}\mathbf{1}_{NK}\mathbf{1}_{NK}^\top$. Since each incidence column satisfies $b_q^\top \mathbf{1}_{NK} = 0$, we have $(P\otimes I_2)A_q = A_q$ and $A_q x = A_q e$. The error system therefore takes the compact form

$$\mathrm{d}e = \big[(P\otimes I_2)h(x) - \alpha(\mathcal{L}\otimes\varsigma)e\big]\mathrm{d}t - \alpha\sum_{q=1}^{m}\eta_q A_q e\,\mathrm{d}W_q(t), \tag{4}$$

where $e = [e^{(k)}]_{k=1}^{K}$ with $e^{(k)} = [e_i^{(k)}]_{i=1}^{N}$. Obviously,

$$(\mathbf{1}_{NK}^\top \otimes I_2)e = \sum_{k=1}^{K}\sum_{i=1}^{N} e_i^{(k)} = \sum_{k=1}^{K}\sum_{i=1}^{N}(x_i^{(k)} - \bar{x}) = \sum_{k=1}^{K}\sum_{i=1}^{N} x_i^{(k)} - NK\bar{x} = \mathbf{0}_2.$$

The following lemmas are presented to facilitate the subsequent analysis.

Lemma 1. Under Assumption 2, for any $x = [x_i]_{i=1}^{NK}$ with $x_i \in \mathbb{R}^2$, the following equation holds:

$$\min_{x\neq 0}\frac{x^\top(\mathcal{L}\otimes\varsigma)x}{x^\top x} = \lambda_2\cdot\sigma_{\min}, \text{ if } \sum_{i=1}^{NK} x_i = \mathbf{0}_2,$$

where $\sigma_{\min} = \min\{1,\sigma\}$ and λ_2 is the second smallest eigenvalue of the super-Laplacian $\mathcal{L}$.

Proof. Based on Assumption 2, the super-Laplacian matrix $\mathcal{L}$ is symmetric and positive semi-definite. Consequently, its eigenvalues can be ordered as $0 = \lambda_1 < \lambda_2 \leqslant \cdots \leqslant \lambda_{NK}$, where the simple zero eigenvalue is associated with eigenvector $\mathbf{1}_{NK}$. Given the diagonal matrix $\varsigma = \mathrm{diag}\{1,\sigma\}$, the properties of the Kronecker product guarantee that the eigenvalues of $\mathcal{L}\otimes\varsigma$ are exactly the pairwise products of the eigenvalues of $\mathcal{L}$ and ς. Thus, the spectrum of $\mathcal{L}\otimes\varsigma$ consists of λ_i and $\lambda_i\sigma$ for $i = 1,\ldots,NK$. The eigenspace associated with the zero eigenvalue is spanned by $\mathbf{1}_{NK}\otimes[1,0]^\top$ and $\mathbf{1}_{NK}\otimes[0,1]^\top$. Excluding this null space, the smallest non-zero eigenvalue of $\mathcal{L}\otimes\varsigma$ is $\min\{\lambda_2,\lambda_2\sigma\} = \lambda_2\sigma_{\min}$. Furthermore, the zero-sum condition $\sum_{i=1}^{NK} x_i = \mathbf{0}_2$ can be equivalently expressed in vector form as $(\mathbf{1}_{NK}^\top\otimes I_2)x = \mathbf{0}_2$. This algebraic relation ensures that the vector x is strictly orthogonal to the null space of $\mathcal{L}\otimes\varsigma$. According to the Rayleigh-Ritz theorem, for any non-zero vector x orthogonal to the eigenspace of the zero eigenvalue, the Rayleigh quotient is bounded below by the smallest non-zero eigenvalue. Therefore, the minimum of this quotient is precisely attained at $\lambda_2\sigma_{\min}$. This completes the proof.

For simplicity, denote $e_t = e(t)$ and $e_0 = e(0)$, and let $\{W_q(t)\}_{q=1}^m$ be the mutually independent standard Wiener processes defined above on a common filtered probability space. To characterize the contributions of the independent noise channels to the Itô correction, define the noise-weighted Laplacian

$$\mathcal{L}_\eta^{[2]} := \mathsf{B}CH^2C\mathsf{B}^\top = \sum_{q=1}^m \eta_q^2 c_q^2 b_q b_q^\top, \text{ where } H = \mathrm{diag}(\eta_1, \ldots, \eta_m).$$

Write $\mu_\eta = \lambda_{\max}(\mathcal{L}_\eta^{[2]})$, $\eta_{\min} = \min_q \eta_q$, $\eta_{\max} = \max_q \eta_q$, and $\sigma_{\max} = \max\{1, \sigma\}$. The following theorem provides a sufficient condition for almost sure exponential convergence of the synchronization errors.

Theorem 1. Under Assumptions 1–3, suppose that $\beta > 0$ and that the solution of (3) with $x_0 \in \mathcal{B}^{NK}$ exists globally and remains in $\mathcal{B}^{NK}$ almost surely. The synchronization errors of (4) converge to zero almost surely at an exponential rate if $\gamma := -\ell + \alpha\lambda_2\sigma_{\min} - \alpha^2\mu_\eta\sigma_{\max}^2 + \frac{\eta_{\min}^2\alpha^2}{m}\lambda_2^2\sigma_{\min}^2 > 0$.

Proof. For $e \neq 0$, take $V(e) = \frac{1}{2}\log(e^\top e)$. Applying Itô's formula to (4) and using Assumption 3 and Lemma 1 and the Cauchy-Schwarz inequality gives

$$\begin{aligned}
V(e_t) =& V(e_0) + \int_0^t \left[\frac{e_s^\top (P \otimes I_2) h(x_s)}{e_s^\top e_s} - \alpha \frac{e_s^\top (\mathcal{L} \otimes \varsigma) e_s}{e_s^\top e_s} + \frac{\alpha^2}{2} \sum_{q=1}^m \eta_q^2 \frac{e_s^\top A_q^2 e_s}{e_s^\top e_s} - \alpha^2 \sum_{q=1}^m \eta_q^2 \frac{(e_s^\top A_q e_s)^2}{(e_s^\top e_s)^2} \right] \mathrm{d}s + M_t \\
\leqslant& V(e_0) + \int_0^t \left[\ell - \alpha\lambda_2\sigma_{\min} + \alpha^2 \frac{e_s^\top (\mathcal{L}_\eta^{[2]} \otimes \varsigma^2) e_s}{e_s^\top e_s} - \frac{\eta_{\min}^2\alpha^2}{m} \Big(\frac{e_s^\top (\mathcal{L} \otimes \varsigma) e_s}{e_s^\top e_s} \Big)^2 \right] \mathrm{d}s + M_t \\
\leqslant& V(e_0) + \left[\ell - \alpha\lambda_2\sigma_{\min} + \alpha^2\mu_\eta\sigma_{\max}^2 - \frac{\eta_{\min}^2\alpha^2}{m}\lambda_2^2\sigma_{\min}^2 \right] t + M_t,
\end{aligned}$$

where

$$M_t = -\alpha \sum_{q=1}^m \eta_q \int_0^t \frac{e_s^\top A_q e_s}{e_s^\top e_s} \, \mathrm{d}W_q(s).$$

Here, $\bar{x} \in \mathcal{B}$, $(P \otimes I_2)e = e$, and $\sum_{k,i} e_i^{(k)} = 0$ give $e^\top (P \otimes I_2) h(x) \leqslant \ell e^\top e$. We also use $\sum_q \eta_q^2 A_q^2 = 2\mathcal{L}_\eta^{[2]} \otimes \varsigma^2$, which follows from $b_q^\top b_q = 2$. Independence of the Wiener processes and $A_q \succeq 0$ yield

$$\langle M_t, M_t \rangle = \alpha^2 \int_0^t \sum_{q=1}^m \eta_q^2 \left(\frac{e_s^\top A_q e_s}{e_s^\top e_s} \right)^2 \mathrm{d}s \leqslant \alpha^2 \eta_{\max}^2 \int_0^t \left(\frac{e_s^\top (\mathcal{L} \otimes \varsigma) e_s}{e_s^\top e_s} \right)^2 \mathrm{d}s \leqslant \alpha^2 \eta_{\max}^2 \lambda_{NK}^2 \sigma_{\max}^2 t.$$

The martingale strong law gives $M_t/t \to 0$ almost surely. Therefore,

$$\limsup_{t\to\infty} \frac{\log \|e_t\|}{t} \leqslant \limsup_{t\to\infty} \left[\frac{V(e_0)}{t} - \gamma + \frac{M_t}{t} \right] = -\gamma < 0, \qquad \text{a.s.}$$

For $e_0 = 0$, invariance of the synchronization manifold gives $e_t = 0$, completing the proof.

The preceding result establishes exponential decay of the synchronization errors. To obtain convergence to x^*, we next analyze the mean state as a perturbed trajectory of the isolated reaction system.

Theorem 2. Under the conditions of Theorem 1, with h continuously differentiable near x^* and $\mathcal{B}$ sufficiently small, system (3) achieves synchronization to the uniform stationary state x^* almost surely as $t \to \infty$ if $\gamma > 0$.

Proof. Every edge noise channel and the deterministic diffusion conserve the sum of node states. Hence the mean state satisfies

$$\dot{\bar{x}} = h(\bar{x}) + r(t), \text{ where } r(t) = \frac{1}{NK} \sum_{k=1}^K \sum_{i=1}^N [h(x_i^{(k)}) - h(\bar{x})], \text{ and } \|r(t)\| \leqslant \frac{L_h}{\sqrt{NK}} \|e(t)\|.$$

Here, L_h is a local Lipschitz constant of h near x^*. By Theorem 1, $r(t)$ decays exponentially almost surely. The limiting isolated system is

$$\dot{y} = h(y), \qquad \dot{y}_u = f(y_u, y_v), \qquad \dot{y}_v = g(y_u, y_v). \tag{5}$$

Assumption 1 guarantees that the isolated system (5) converges locally at an exponential rate to the uniform stationary state x^*. Since $r(t)$ decays exponentially and $\bar{x}(t)$ remains in a sufficiently small neighborhood of x^*, the average state $\bar{x}$ approaches x^* almost surely. Together with the convergence of the synchronization errors to zero, this ensures that the stochastic system (3) ultimately synchronizes to the uniform stationary state x^* almost surely.

Corollary 1. Under the conditions of Theorem 2, suppose that all edge noise intensities are equal, $\eta_q = \eta \geqslant 0$. Define

$$\mathcal{L}^{[2]} := \mathsf{B}C^2\mathsf{B}^\top = \mathcal{L}^L + \left(\frac{\beta}{\alpha}\right)^2 \mathcal{L}^I, \qquad \mu_{NK} := \lambda_{\max}(\mathcal{L}^{[2]}).$$

All node states converge to the uniform stationary state x^* almost surely, and the synchronization errors decay exponentially, if $\gamma_{\text{ind}} := -\ell + \alpha\lambda_2\sigma_{\min} - \eta^2\alpha^2(\mu_{NK}\sigma_{\max}^2 - \frac{\lambda_2^2\sigma_{\min}^2}{m}) > 0$.

Proof. The result follows directly from Theorems 1 and 2 by setting $\eta_q = \eta$ for all edges, and the proof is omitted.

The criterion separates reaction, diffusion, and noise contributions while retaining their dependence on network topology. The constant ℓ bounds the reaction contribution, while λ_2 measures algebraic connectivity and controls the weakest diffusive dissipation through $\alpha\lambda_2\sigma_{\min}$. The largest eigenvalue λ_{NK} gives the full spectral span and bounds the martingale quadratic variation. For mutually independent edge noise processes, the stochastic correction instead involves μ_{NK}, the largest eigenvalue of the Laplacian with squared edge weights, rather than the matrix square of $\mathcal{L}$. This correction depends jointly on η, diffusion parameters, and network spectra, with inter-layer coupling entering through $\mathcal{L}$ and $\mathcal{L}^{[2]}$. For $NK > 3$, increasing uniform noise intensity at fixed topology and diffusion lowers γ_{ind} and makes the sufficient convergence condition more restrictive. The criterion thus provides an analytical benchmark for these coupled effects, rather than implying that stronger connectivity always improves stability.

Under its assumptions, Theorem 2 guarantees convergence to the uniform stationary state and therefore excludes persistent spatial patterns. However, failure of this sufficient condition does not establish Turing instability or locate its threshold. The numerical study complements this stability analysis by examining how noise, diffusion, and multiplex structure jointly affect pattern onset and persistence through the forward and backward transitions.

4 Turing instability

Moving forward, the Turing instability is investigated through numerical simulation. The Mimura-Murray prey-predator model is used to describe the local dynamics, which is given by

$$\begin{aligned}\dot{u}_i &= \left(\frac{a + bu_i - u_i^2}{c} - v_i\right) u_i,\\ \dot{v}_i &= (u_i - (1 + dv_i))v_i,\end{aligned}$$

where $a = 35$, $b = 16$, $c = 9$, $d = 0.4$ are the fixed system parameters, so that the model possesses a unique positive coexistence equilibrium $(u^*, v^*) = (5, 10)$. The following order parameter is used to quantify the degree of synchronization

$$A(\sigma) = \left\{\frac{1}{NK}\sum_{i=1}^{N}\sum_{k=1}^{K}\left[(u_i^{(k)} - u^*)^2 + (v_i^{(k)} - v^*)^2\right]\right\}^{1/2}.$$

Following the amplitude measure used in [24,46], we introduce normalization by NK to obtain a root-mean-square deviation per node, facilitating comparisons of pattern amplitudes across different network sizes and numbers of layers.

In simulation, unless otherwise specified, the ER random network [49] is adopted as the intra-layer topology with the network size $N = 200$ and the connection probability $p = 0.03$, and a complete graph governs the inter-layer topology. The multiplex network consists of $K = 5$ independently generated layers. The diffusion coefficient is fixed at $\alpha = 0.05$. Rather than being assigned an independent value, the inter-layer diffusion coefficient is proportionally defined as $\beta = 0.1\alpha$. All edge noise intensities are equal, $\eta_q = \eta$, with the default value $\eta = 0.1$. To simulate the forward transition, the initial node states are configured as small random perturbations around the uniform stationary state. Conversely, for the backward transition, the system is initialized using the final simulated states of a trajectory generated at $\sigma = 100$, where established Turing patterns are observed.

4.1 Noise-induced shifts in transition thresholds and hysteresis

The influence of noise on the system's global stability is characterized in Figure 2. In the deterministic limit ($\eta = 0$), the order parameter A exhibits a discontinuous hysteresis loop as shown in Figure 2(a), consistent with a subcritical Turing transition. In this deterministic case, simulations initialized near the uniform state and from an established pattern yield different final states within $\sigma \in (\sigma_c^b, \sigma_c^f)$, providing numerical evidence of initial-condition-dependent state selection. In Figure 2(a), the forward transitions at $\eta = 0.9$ and 1.0 occur at smaller diffusion ratios than in the

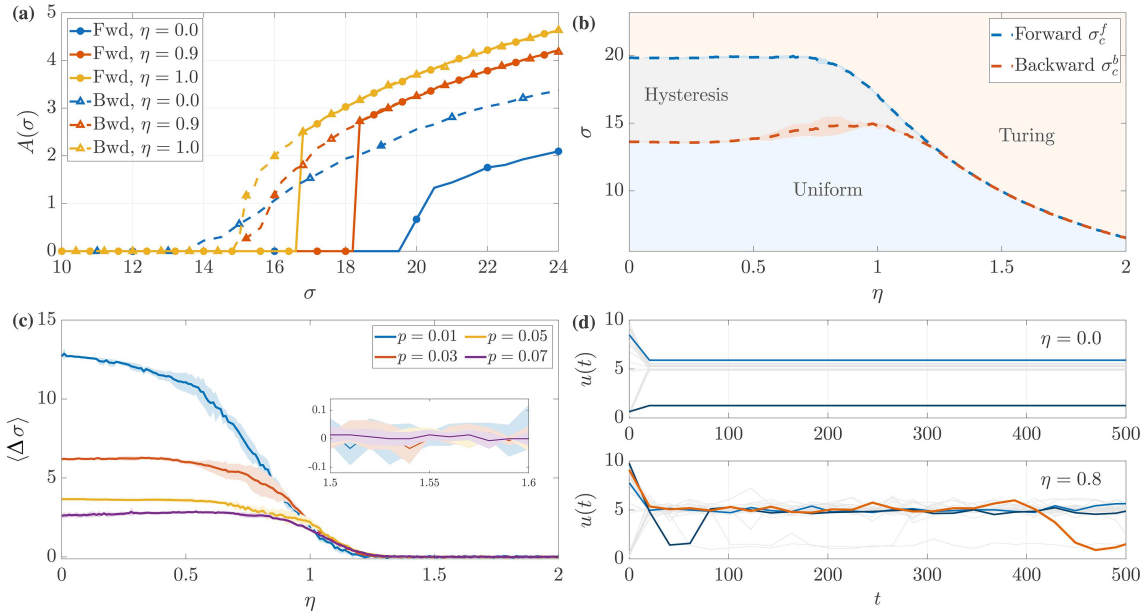

Figure 2 (Color online) Multiplicative noise modifies the thresholds for Turing pattern onset and reduces the hysteresis width. (a) The evolution of the order parameter $A(\sigma)$ as the diffusion ratio σ increases (forward, denoted Fwd) and decreases (backward, denoted Bwd) for different noise intensities, showing a clear hysteresis loop. (b) The forward and backward critical values of σ for varying noise intensities η, with dashed curves and shaded bands representing the means and one sample standard deviation, respectively, over ten independent simulations with different random seeds at each noise intensity. (c) The mean hysteresis width $\langle \Delta\sigma \rangle$ as a function of η for ER connection probabilities $p = 0.01$, 0.03, 0.05, and 0.07. Curves and shaded bands represent the means and one sample standard deviation over ten independent simulations with different random seeds. The inset enlarges the near-zero threshold separation. (d) Temporal trajectories of the activator density u in the first layer at $\eta = 0.0$ and 0.8, illustrating noise-induced fluctuations and transitions of individual nodes from an activator-rich state to a depleted state.

deterministic case. The separation between the forward and backward transitions also narrows as noise increases, indicating a reduced hysteresis interval.

As shown in Figure 2(b), weak noise produces only small changes in the forward and backward critical thresholds. The forward critical threshold σ_c^f shows a slight initial increase followed by a pronounced decrease, indicating a non-monotonic effect of noise on pattern onset. This contrasts with the monotonic effects of noise reported under specific formulations in previous studies [46,47], highlighting that the influence of noise on Turing instability depends on its formulation. At stronger noise intensities, the backward critical threshold σ_c^b also decreases, indicating that established Turing patterns persist at smaller diffusion ratios. The separation between the two thresholds narrows with increasing noise intensity, reducing the hysteresis interval.

To quantify this reduction, Figure 2(c) shows the mean hysteresis width $\langle \Delta\sigma \rangle$, where $\Delta\sigma = \sigma_c^f - \sigma_c^b$, for four ER connection probabilities. Connectivity affects the width at weak noise, but the mean width decreases substantially and approaches zero in all four cases as noise increases, although individual realizations may retain a nonzero threshold separation.

The temporal characteristics of these noise-driven dynamics are further illustrated in Figure 2(d). The time evolution of node densities shown in Figure 2(d) reveals a significant contrast: while the deterministic case ($\eta = 0$) remains perfectly stable on the pattern branch, the introduction of multiplicative noise ($\eta = 0.8$) triggers stochastic transitions of node states between the high- and low-density manifolds.

4.2 Interplay of diffusion, inter-layer coupling, and noise

In the following, we investigate the collective impact of the diffusion coefficient α and the inter-layer coupling ratio β/α on the system stability. As illustrated in Figure 3(a), for a relatively low diffusion coefficient ($\alpha = 0.03$), both the forward and backward critical thresholds (σ_c^f, σ_c^b) decrease monotonically with β/α, and the hysteresis loop gradually shrinks. This suggests that, in this regime, inter-layer coupling acts as a facilitator for the emergence of Turing patterns. However, a qualitative transition occurs as the internal diffusion increases. For $\alpha = 0.05$ and 0.10 (Figures 3(b) and (c)), the critical points exhibit a non-monotonic dependence on the coupling ratio. Specifically, after an initial decrease or weak variation, the forward threshold rises with β/α, indicating that strong inter-layer coupling can suppress pattern formation at higher internal diffusion levels, before eventually reaching a saturation plateau at large β/α.

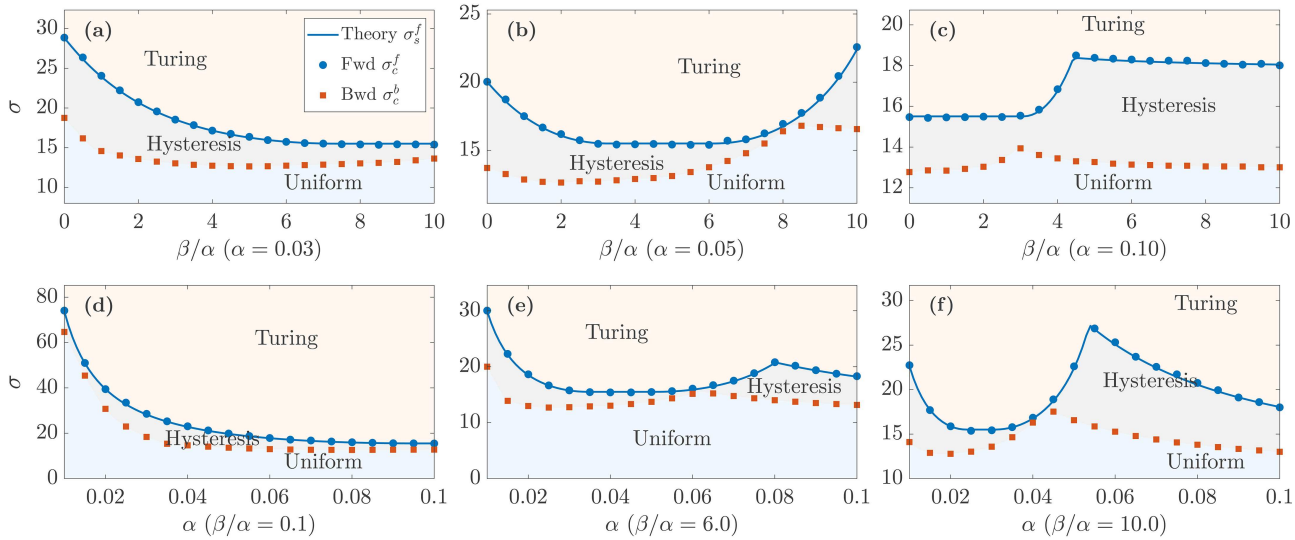

Figure 3 (Color online) The multiplex network architecture exerts a complex non-monotonic influence on the Turing phase transitions and modulates the hysteresis interval. (a)–(c) The phase diagrams delineating the forward critical boundary σ_c^f and the backward critical boundary σ_c^b against the inter-layer coupling β/α for fixed diffusion rates α. (d)–(f) The phase diagrams mapping the critical thresholds against the diffusion rates α under fixed inter-layer coupling β/α. Solid blue curves represent the theoretical forward thresholds σ_s^f obtained from the linear stability analysis of the deterministic system. Blue circles and orange squares denote the simulated forward and backward thresholds σ_c^f and σ_c^b, respectively.

The effect of α on the emergence of Turing patterns is shown in Figures 3(d)–(f). When the inter-layer coupling ratio is small ($\beta/\alpha = 0.1$), both σ_c^f and σ_c^b decrease rapidly as α increases and then stabilize at a low plateau. This indicates that, for weakly coupled layers, the intra-layer diffusion α facilitates the onset of Turing patterns by lowering the required diffusion ratio σ. However, as the inter-layer coupling becomes dominant ($\beta/\alpha = 6.0$ or 10.0), a distinct non-monotonic behavior is observed. While the backward threshold σ_c^b remains relatively stable, the forward threshold σ_c^f exhibits a prominent peak, leading to a significantly widened hysteresis interval. The results shown in Figures 3(d)–(f) clearly demonstrate that the presence of inter-layer coupling fundamentally alters the influence of diffusion on the Turing instability.

To explain the forward transition, we consider the supra-Laplacian modes $\mathcal{L}\phi_q = \lambda_q\phi_q$, where λ_q and ϕ_q are the eigenvalues and eigenvectors for $q = 1, \ldots, NK$. Linearization of the deterministic system around the uniform stationary state gives $M_q = J - \alpha\lambda_q\varsigma$, where J is the Jacobian of the local reaction dynamics at this state. The modal growth rate is $\rho_q(\sigma) = \max \mathrm{Re}[\mathrm{eig}(M_q)]$. The theoretical forward threshold σ_s^f is the first crossing of $\max_{\lambda_q>0} \rho_q(\sigma)$ from negative to positive as σ increases. The eigenvalue and eigenvector of a critical nonuniform mode attaining zero growth rate at this threshold are denoted by λ_* and ϕ_*. The spectral predictions closely match the simulated forward thresholds in Figure 3 and reproduce their non-monotonic dependence on diffusion and inter-layer coupling.

For the present reaction kinetics, the single-mode instability threshold is $\sigma_s(\lambda) = (110/3+4\alpha\lambda)/[\alpha\lambda(10/3-\alpha\lambda)]$ for $0 < \alpha\lambda < 10/3$, with its minimum attained at λ_{opt}. In Figure 4(a), λ_* lies near this optimum at weak coupling, giving a low forward threshold. As coupling increases, λ_* moves away from the optimum, and the threshold rises. A switch of the critical mode is followed by weak variation in λ_*, consistent with threshold saturation. The corresponding eigenvector in Figure 4(b) has similar spatial profiles across layers and large components concentrated at a few nodes, indicating localization at pattern onset. This linear criterion does not determine the backward threshold, which concerns the persistence of established nonlinear patterns.

Figures 4(c)–(e) show the joint influence of noise intensity η and inter-layer coupling ratio β/α. The forward threshold depends non-monotonically on coupling at weak noise but decreases with coupling at stronger noise. Increasing noise generally lowers both transition thresholds and narrows the hysteresis interval. To quantify the departure from additive effects on the forward threshold, we define

$$I_f(\eta, \beta/\alpha) = \sigma_c^f(\eta, \beta/\alpha) - \sigma_c^f(0, \beta/\alpha) - \sigma_c^f(\eta, 0) + \sigma_c^f(0, 0). \tag{6}$$

Additive effects relative to the baseline $(\eta, \beta/\alpha) = (0, 0)$ would give $I_f = 0$. The predominantly negative values in Figure 4(f) at moderate to strong coupling indicate that the joint forward threshold is lower than the additive prediction.

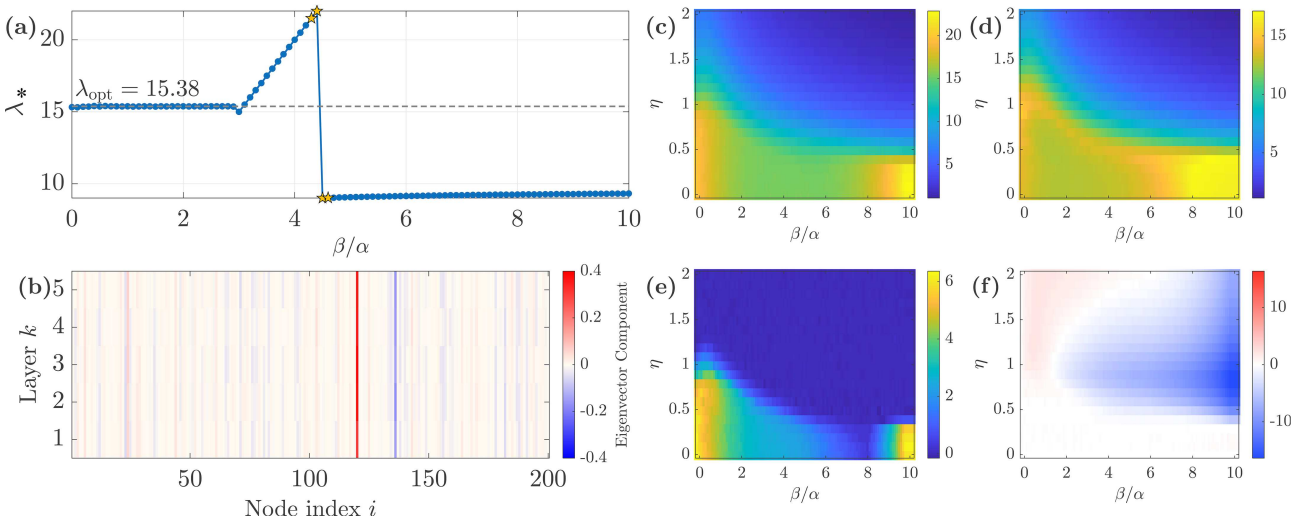

Figure 4 (Color online) Spectral properties at pattern onset and joint effects of noise and inter-layer coupling. With $\alpha = 0.1$, (a) critical eigenvalue λ_* versus β/α, with the dashed line marking $\lambda_{\rm opt} \approx 15.38$ and stars marking $\beta/\alpha = 4.3$, 4.4, 4.5, and 4.6. (b) Unit-norm critical eigenvector at $\beta/\alpha = 4.5$. With $\alpha = 0.05$, (c)–(f) forward threshold, backward threshold, hysteresis width, and interaction index I_f defined in (6), respectively, over the noise-coupling parameter plane.

4.3 Topological dependence and scale robustness of pattern onset

To examine how network structure affects pattern onset and persistence, we compare multiplex networks with ER [49], WS [50], and BA [51] intra-layer topologies while varying the mean intra-layer degree, the intra-layer network size, and the number of layers. Here, Pure-ER denotes a multiplex whose intra-layer networks are independently sampled from the ER model with identical parameters. Pure-WS and Pure-BA are defined analogously.

Figure 5(a) shows that the forward threshold decreases markedly with increasing mean intra-layer degree in Pure-ER and Pure-WS networks, whereas its variation is comparatively small in Pure-BA networks. Changing the network size has little effect on the thresholds in Pure-ER and Pure-WS networks. In Pure-BA networks, however, a larger network yields a lower forward threshold at small mean degrees, while this size dependence diminishes as connectivity increases. The critical eigenvalues in Figure 5(d) provide a spectral interpretation of these trends. As the mean degree increases, the critical eigenvalues in Pure-ER and Pure-WS networks increase, thereby lowering the diffusion ratio required for pattern onset. In contrast, the critical eigenvalues in Pure-BA networks remain close across different degrees, consistent with their comparatively stable forward thresholds. The critical spectral positions also show limited dependence on network size, with modest differences in Pure-BA networks at low mean degrees. The backward thresholds vary less than the forward thresholds, so the hysteresis intervals in Pure-ER and Pure-WS networks contract substantially as connectivity increases, as shown in Figure 5(c).

Figures 5(b) and (e) further show that the influence of layer number depends on the inter-layer architecture. We compare nearest-neighbor ring coupling with all-to-all coupling, denoted by ring and ALL, respectively. Increasing K preserves the inter-layer degree at two for ring, whereas it increases that degree to $K-1$ for ALL. Thus, the ALL comparison changes both the number of layers and the inter-layer connectivity at fixed coupling strength per edge. The forward threshold in Pure-ER networks decreases with increasing K, particularly under ALL coupling, and Pure-WS networks exhibit a similar decrease under ALL coupling. These trends are consistent with the shifts in critical spectral position shown in Figure 5(e). By contrast, the Pure-WS forward threshold changes little under ring coupling, where the inter-layer degree remains fixed. Pure-BA networks retain weak sensitivity to the number of layers under both architectures. Even under ALL coupling, the critical eigenvalue varies by no more than 0.754 across the sampled layer numbers, while the forward threshold remains nearly unchanged.

To quantify the localization illustrated in Figure 4(b), Figure 5(f) compares the cumulative weight $C(f)$ of the critical eigenspace on the highest-degree fraction f of nodes across network topologies. Let m_* denote the multiplicity of the critical eigenvalue λ_*, and let $U_* \in \mathbb{R}^{NK\times m_*}$ be an orthonormal basis for its eigenspace. The normalized weight assigned to node i, summed over its K layer replicas, is

$$C(f) = \sum_{j=1}^{fN} w_{\pi(j)}, \ \text{where } w_i = \frac{1}{m_*}\sum_{k=1}^{K}\sum_{q=1}^{m_*}\left|(U_*)_{(k-1)N+i,q}\right|^2 \ \text{and} \ \sum_{i=1}^{N} w_i = 1. \tag{7}$$

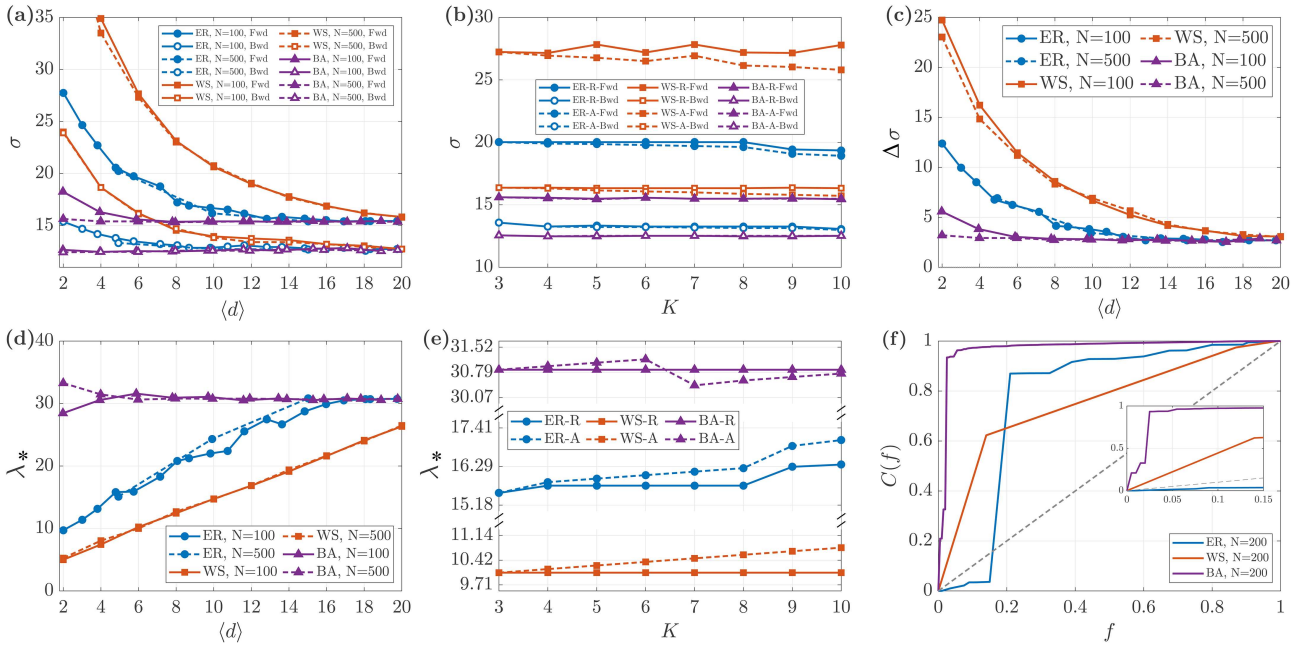

Figure 5 (Color online) Transition thresholds and critical spectral modes across multiplex network topologies. (a) Forward and backward thresholds versus the measured mean intra-layer degree for $N = 100, 500$, with $K = 5$ and ALL inter-layer coupling. (b) Thresholds versus K for ring and ALL coupling, with $N = 200$ and nominal mean intra-layer degree six. (c) Hysteresis width $\Delta\sigma = \sigma_c^f - \sigma_c^b$. (d) and (e) deterministic critical eigenvalues λ_* for the configurations in (a) and (b); breaks in (e) omit empty spectral intervals. (f) Cumulative critical-eigenspace weight $C(f)$ on nodes ranked by decreasing mean intra-layer degree, for $N = 200$, $K = 5$, nominal mean degree six, and ALL coupling; the inset enlarges $f \leqslant 0.15$. Ring denotes nearest-neighbor ring coupling, and ALL denotes all-to-all coupling.

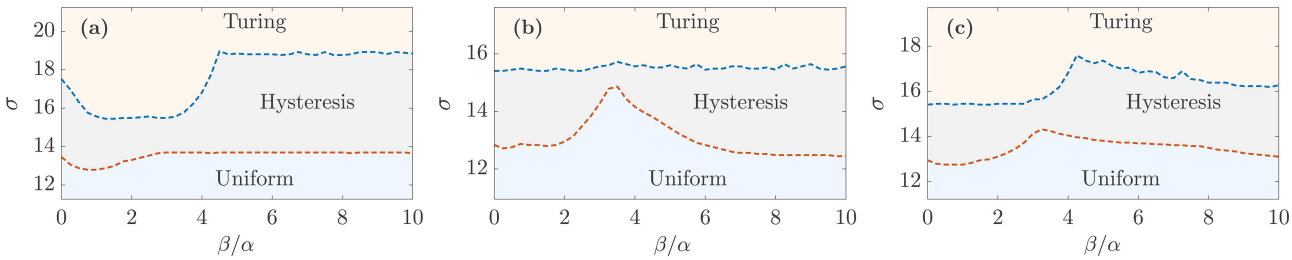

Figure 6 (Color online) Inter-layer coupling responses in multiplex networks with different layer compositions. Forward and backward transition thresholds versus the inter-layer coupling ratio β/α for (a) Pure-WS networks, (b) Pure-BA networks, and (c) a heterogeneous network comprising two WS, two ER, and one BA layer.

Here, $d_i^{(k)}$ denotes the intra-layer degree of node i in layer k, and $\bar{d}_i = \frac{1}{K}\sum_{k=1}^{K} d_i^{(k)}$ is its mean degree across the K layers, and π orders nodes by decreasing $\bar{d}_i$ such that $\bar{d}_{\pi(1)} \geqslant \cdots \geqslant \bar{d}_{\pi(N)}$. This strong hub localization provides a spectral explanation for the weak scale sensitivity observed in Pure-BA networks. Specifically, the highest-degree 10% of nodes carry approximately 97.30% of the dominant-mode energy, indicating that the onset of Turing instability is governed predominantly by a small number of hub nodes rather than by the network as a whole. Consequently, variations in network size, layer number, or average connectivity may have only limited influence on the critical threshold as long as this localized spectral structure is preserved. This behavior differs markedly from Pure-ER and Pure-WS networks, where the dominant-mode energy is distributed over a substantially broader fraction of nodes and is therefore more sensitive to global structural changes.

To further examine the robustness of Pure-BA networks, Figure 6 compares the responses to inter-layer coupling in Pure-WS, Pure-BA, and a heterogeneous network comprising two WS, two ER, and one BA layer, using the same diffusion coefficient as in Figure 3(c). As in the Pure-ER case in Figure 3(c), the forward threshold in the Pure-WS network exhibits a pronounced non-monotonic dependence on inter-layer coupling strength and approaches a plateau in the strong-coupling regime. The heterogeneous network also exhibits a pronounced non-monotonic response. In contrast, the forward threshold in the Pure-BA network remains nearly constant throughout the sampled coupling range, demonstrating that the influence of inter-layer coupling on pattern onset depends strongly on the intra-layer topology.

Together with the weak dependence on network size, mean degree, and layer number in Figure 5, these results show that the robustness of the forward threshold in the Pure-BA network extends to variations in inter-layer coupling strength. This behavior is consistent with the localization of the critical mode on a small set of hub nodes, suggesting that a local structural core governs pattern onset and limits its sensitivity to changes in global network structure and coupling. The heterogeneous network does not exhibit the same robustness, indicating that a single BA layer is insufficient to reproduce the Pure-BA response in the configuration considered. The backward threshold in the Pure-BA network nevertheless varies with coupling. Hence, the observed scale robustness and coupling insensitivity pertain primarily to the forward transition.

5 Conclusion

Recognizing that real-world populations and substances naturally disperse across interconnected layers, such as species migrating across multiple habitats, we constructed a multiplex-networked activator-inhibitor system model to capture these cross-layer interactions and diffusion processes. Given that diffusive processes are inevitably subject to intrinsic fluctuations, we incorporated multiplicative noise driven by mutually independent edge noise processes into the model, thereby establishing a multiplex-networked stochastic reaction-diffusion system model. In contrast to other studies that assume additive noise [39, 45] or noise intensity tied to the difference from a homogeneous stationary state [46], we consider the situation in which the intensity of multiplicative noise is proportional to the local density differences between a node and its intra- and inter-layer neighbors, which more accurately aligns with realistic scenarios.

Analytically, by employing the stability theory of stochastic differential equations, we derived a sufficient condition for almost sure convergence to the uniform stationary state. The numerical simulations on the Mimura-Murray model revealed that multiplicative noise has a non-monotonic influence on pattern onset. Specifically, we demonstrated that weak noise can slightly raise the forward threshold, whereas stronger noise lowers the transition thresholds and reduces the observed hysteresis width.

Furthermore, we systematically explored the impact of the multiplex architecture by varying the intra-layer diffusion coefficient and the inter-layer coupling strength. While intra-layer diffusion promotes pattern onset at weak inter-layer coupling, its effect can become non-monotonic at stronger coupling. We demonstrated that inter-layer coupling also exhibits a complex, non-monotonic influence. Specifically, we show that, when intra-layer diffusion is weak, enhancing inter-layer coupling facilitates pattern formation, whereas when diffusion dominates, increasing inter-layer coupling can suppress the emergence of Turing patterns. Furthermore, we found that in the Pure-ER configurations examined, this suppression primarily elevates the forward critical threshold, which governs the transition from the synchronous state to the Turing pattern, with smaller changes in the backward threshold. This asymmetric effect can widen the observed hysteresis interval. Interestingly, the critical thresholds may also exhibit saturation at strong inter-layer coupling under certain parameter settings. Finally, from a topological perspective, we found pronounced robustness of the forward threshold across the examined Pure-BA configurations. We found that in these scale-free architectures, the threshold for the onset of Turing patterns is predominantly governed by hub-localized critical modes and consequently remains comparatively robust to changes in connectivity, network size, layer number, and inter-layer coupling. This robust behavior contrasts with the greater sensitivity to connectivity and inter-layer architecture observed in Pure-ER and Pure-WS networks.

Our results further extend the deterministic multiplex framework of [38] in several respects. In addition to incorporating state-dependent multiplicative noise into the multiplex-networked activator-inhibitor system, we extend the investigation of multiplex effects in both the network dimension and the inter-layer coupling regime. Although the theoretical formulation in [38] accommodates multiplex networks with an arbitrary number of layers, the numerical analysis was primarily demonstrated for two-layer networks, whereas here we explore Turing pattern formation in multiplex networks with varying numbers of layers. More importantly, while their perturbative analysis of inter-layer coupling is developed in the weak-coupling regime, our theoretical treatment eliminates this assumption, allowing us to investigate a substantially broader coupling regime. This reveals qualitatively distinct behavior that, even with the local dynamical parameters fixed, varying the inter-layer coupling strength can exert a non-monotonic influence on Turing pattern formation. Moreover, under certain parameter settings, the critical thresholds may exhibit saturation at strong coupling.

Ultimately, our findings provide a deeper theoretical understanding of how the subtle interplay between multi-layer network topologies and stochastic fluctuations drives cross-layer pattern formation. Future research could extend this framework to incorporate directed multiplex networks or time-varying topologies, bringing the mathematical modeling even closer to the dynamic realities of complex ecological and biological systems.

Acknowledgements This work was supported by National Natural Science Foundation of China (Grant Nos. U2541220, 12671613, 12271519), Basic Research Program of Jiangsu (Grant No. BK20253020), Jiangsu Provincial Scientific Research Center of Applied Mathematics (Grant No. BK20233002), Shenzhen Science and Technology Program (Grant No. JCYJ20240813101300001), Fundamental Research Funds for the Central Universities (Grant Nos. 2023ZDYQ11005, 2024KYJD2002), and Research Grants Council of Hong Kong (Grant No. CityU 11201924).

References

1 Cai R Y, Zhou H C, Kou C H. Active disturbance rejection control for fractional reaction-diffusion equations with spatially varying diffusivity and time delay. Sci China Inf Sci, 2022, 65: 129203
2 Singh A K, Almshekhs R, Kumar M, et al. The emergence of Turing instability and pattern formation in a nonlinear stochastic spatiotemporal epidemic model with reinfections. Acta Biotheor, 2026, 74: 10
3 Ninomiya H. Example of Turing's instability by equal diffusion. J Differ Equ, 2024, 392: 255–265
4 Tompkins N, Li N, Girabawe C, et al. Testing Turing's theory of morphogenesis in chemical cells. Proc Natl Acad Sci USA, 2014, 111: 4397–4402
5 Biancalani T, Fanelli D, Di Patti F. Stochastic Turing patterns in the Brusselator model. Phys Rev E, 2010, 81: 046215
6 Liu Q X, Doelman A, Rottschäfer V, et al. Phase separation explains a new class of self-organized spatial patterns in ecological systems. Proc Natl Acad Sci USA, 2013, 110: 11905–11910
7 Giunta G, Seyed-Allaei H, Gerland U. Cross-diffusion induced patterns for a single-step enzymatic reaction. Commun Phys, 2020, 3: 167
8 Turing A M. The chemical basis of morphogenesis. Philos Trans R Soc London Ser B Biol Sci, 1952, 237: 37–72
9 Gierer A, Meinhardt H. A theory of biological pattern formation. Kybernetik, 1972, 12: 30–39
10 Pigani E, Sgarbossa D, Suweis S, et al. Delay effects on the stability of large ecosystems. Proc Natl Acad Sci USA, 2022, 119: 2203498119
11 Grilli J, Barabási G, Michalska-Smith M J, et al. Higher-order interactions stabilize dynamics in competitive network models. Nature, 2017, 548: 210–213
12 Sun Y Z, Leng S Y, Lai Y C, et al. Closed-loop control of complex networks: a trade-off between time and energy. Phys Rev Lett, 2017, 119: 198301
13 Jiang S, Zhou J, Small M, et al. Searching for key cycles in a complex network. Phys Rev Lett, 2023, 130: 187402
14 Qin B W, Sheng W, Qian X, et al. Reordered hierarchical complexity in ecosystems with delayed interactions. Proc Natl Acad Sci USA Nexus, 2025, 4: 214
15 Yang Z X, Wang L, Wang X F, et al. Controllability of heterogeneous networked sampled-data systems. Sci China Inf Sci, 2025, 68: 132207
16 Niu T M, Mao B, Wang L J, et al. Non-trivial consensus control on directed signed networks. Sci China Inf Sci, 2026, 69: 132203
17 Xiao R, Wen G, Han J, et al. Complexity and delay shape oscillatory transitions in complex networks. Natl Sci Rev, 2026, 13: 608
18 Sun Y, Wang H, Liu X, et al. Networked collective dynamics in animal ecology and cell biology. Phys Life Rev, 2026, 57: 4–60
19 Othmer H G, Scriven L E. Instability and dynamic pattern in cellular networks. J Theor Biol, 1971, 32: 507–537
20 Othmer H G, Scriven L E. Non-linear aspects of dynamic pattern in cellular networks. J Theor Biol, 1974, 43: 83–112
21 Horsthemke W, Lam K, Moore P K. Network topology and Turing instabilities in small arrays of diffusively coupled reactors. Phys Lett A, 2004, 328: 444–451
22 Moore P K, Horsthemke W. Localized patterns in homogeneous networks of diffusively coupled reactors. Physica D-Nonlinear Phenomena, 2005, 206: 121–144
23 Gallos L K, Argyrakis P. Absence of kinetic effects in reaction-diffusion processes in scale-free networks. Phys Rev Lett, 2004, 92: 138301
24 Nakao H, Mikhailov A S. Turing patterns in network-organized activator-inhibitor systems. Nat Phys, 2010, 6: 544–550
25 Asllani M, Challenger J D, Pavone F S, et al. The theory of pattern formation on directed networks. Nat Commun, 2014, 5: 4517
26 Van der Kolk J, García-Pérez G, Kouvaris N E, et al. Emergence of geometric Turing patterns in complex networks. Phys Rev X, 2023, 13: 021038
27 Li B, Zhu L. Turing instability analysis of a reaction-diffusion system for rumor propagation in continuous space and complex networks. Inf Process Manage, 2024, 61: 103621
28 Zheng Q, Shen J, Pandey V, et al. Turing instability in a network-organized epidemic model with delay. Chaos Solitons Fract, 2023, 168: 113205
29 He L, Su H. Turing pattern of an SIRI model on large-scale homogeneous and heterogeneous networks. Nonlinear Dyn, 2023, 111: 16605–16626
30 Del Genio C I, Gómez-Gardeñes J, Bonamassa I, et al. Synchronization in networks with multiple interaction layers. Sci Adv, 2016, 2: 1601679
31 Shi L, Zhou J, Ye Y. Pattern formation in a predator-prey model with Allee effect and hyperbolic mortality on multiplex networks. Mathematics, 2023, 11: 3339
32 Ye Y, Zhou J, Zhao Y. Pattern formation in reaction-diffusion information propagation model on multiplex simplicial complexes. Inf Sci, 2025, 689: 121445
33 Zhao B, Shen J. Navigating epidemic spread through multiplex networks: unveiling Turing instability and cross-diffusion dynamics. Physica A-Statistical Mech its Appl, 2025, 660: 130312
34 Fu S C, Peng Q M, He Y, et al. Unsupervised multiplex graph diffusion networks with multi-level canonical correlation analysis for multiplex graph representation learning. Sci China Inf Sci, 2025, 68: 132102

35 Zhao T T, Huang J, Wang Y B, et al. Saturation function-based intermittent control on fixed-time output synchronization of multilayered networks. Sci China Inf Sci, 2025, 68: 209201

36 Li X J, Li C, Li X. The impact of information dissemination on vaccination in multiplex networks. Sci China Inf Sci, 2022, 65: 172202

37 Gong Y D, Yang S H, Liu S Y, et al. Strategies for mitigating detrimental effects in cyber-physical multiplex networks. Sci China Inf Sci, 2024, 67: 169201

38 Asllani M, Busiello D M, Carletti T, et al. Turing patterns in multiplex networks. Phys Rev E, 2014, 90: 042814

39 Asllani M, Biancalani T, Fanelli D, et al. The linear noise approximation for reaction-diffusion systems on networks. Eur Phys J B, 2013, 86: 476

40 Biancalani T, Jafarpour F, Goldenfeld N. Giant amplification of noise in fluctuation-induced pattern formation. Phys Rev Lett, 2017, 118: 018101

41 Di Patti F, Ugartechea Chirino Y, Arbel-Goren R, et al. Stochastic Turing patterns of trichomes in Arabidopsis leaves. Proc Natl Acad Sci USA, 2023, 120: 2309616120

42 Avitabile D, MacLaurin J. Neural fields and noise-induced patterns in neurons on large disordered networks. SIAM J Appl Math, 2026, 86: 427–456

43 Butler T, Goldenfeld N. Robust ecological pattern formation induced by demographic noise. Phys Rev E, 2009, 80: 030902

44 Butler T, Goldenfeld N. Fluctuation-driven Turing patterns. Phys Rev E, 2011, 84: 011112

45 Karig D, Martini K M, Lu T, et al. Stochastic Turing patterns in a synthetic bacterial population. Proc Natl Acad Sci USA, 2018, 115: 6572–6577

46 Xiao R, Gao Q, Azaele S, et al. Effects of noise on the critical points of Turing instability in complex ecosystems. Phys Rev E, 2023, 108: 014407

47 Khan Q, Suen A, Tang B Q. Turing instability suppressed and induced by multiplicative noise in Brusselator system. Commun Nonlinear Sci Numer Simul, 2025, 151: 109092

48 Solé-Ribalta A, De Domenico M, Kouvaris N E, et al. Spectral properties of the Laplacian of multiplex networks. Phys Rev E, 2013, 88: 032807

49 Erdős P, Rényi A. On the evolution of random graphs. Publ Math Inst Hung Acad Sci, 1960, 5: 17–60

50 Watts D J, Strogatz S H. Collective dynamics of 'small-world' networks. Nature, 1998, 393: 440–442

51 Barabási A L, Albert R. Emergence of scaling in random networks. Science, 1999, 286: 509–512